ARTICLE

Check for updates

Havre 2012 pink pumice is evidence of a short-lived, deep-sea, magnetite nanolite-driven explosive eruption

Joseph Knafelc [1✉], Scott E. Bryan [1], Michael W. M. Jones [2], David Gust[1], Guil Mallmann[3], Henrietta E. Cathey[1,2], Andrew J. Berry [3], Eric C. Ferré[4] & Daryl L. Howard[5]

The Havre 2012 deep-sea rhyolite eruption went unobserved and was initially recognised from a massive pumice raft at the sea surface. Havre pumices are predominantly white or grey, however pink pumice is common in the raft. In subaerial explosive eruptions, pink pumice is understood to result from high-temperature atmospheric iron-oxidation. The presence of pink pumice questions the effusive eruption model for the Havre raft. Here we report results from X-ray Absorption Near Edge Structure spectroscopy, magnetic measurements, TEM imaging and glass chemistry that collectively show the colour results from increasing amounts of magnetite nanolites in the raft pumice glass oxidizing to hematite. This suggests a short-lived but powerful explosive eruption phase penetrated the water column allowing hot pyroclasts to oxidise in air. Our results therefore challenge the known depth limits for explosive eruptions in the marine realm and suggest pink pumice can be an indicator of magnetite nanolite-driven explosive eruptions.

[1] School of Earth & Atmospheric Sciences, Queensland University of Technology, Brisbane, QLD, Australia. [2] Central Analytical Research Facility, Queensland University of Technology, Brisbane, QLD, Australia. [3] Research School of Earth Sciences, Australian National University, Canberra, ACT, Australia. [4] School of Geosciences, University of Louisiana at Lafayette, Lafayette, LA, USA. [5] Australian Synchrotron, ANSTO, Clayton, VIC, Australia.
✉email: joseph.knafelc@hdr.qut.edu.au

In silicic subaerial explosive eruptions, magma originating from mid to upper-crustal chamber depths (~3–15 km) at high temperatures (~700–1000 °C) can be ejected into the atmosphere as pyroclastic material, mostly pumice and ash in a matter of seconds to minutes[1–3]. Silicic pumice, which is formed by quenching of gas-rich highly vesiculated magma is typically white or grey, however, pink pumice is reported from some subaerial explosive eruptions[4–7]. Pink pumice has been experimentally produced by exposing pumice to high temperatures (>700 °C) in oxygen-rich environments[5,8]. Natural pink pumice is therefore believed to be the result of exposure of hot pyroclasts to air during subaerial eruptions[4–6,8–10]. Due to the relatively short time pyroclasts are exposed to atmospheric oxygen conditions at high temperatures compared to oxygen diffusion rates in glass[11], we hypothesize that the pink colourisation is likely due to oxidation of magnetite microlites or nanolites to hematite. Magnetite nanolites have recently been identified as having an important role in enhancing magma fragmentation and eruption explosivity as nanolite crystallization upon magma ascent triggers rapid increases in melt viscosity and bubble nucleation[12–22]. These studies have focused on subaerial eruptions but whether nanolites exist and can similarly promote increased melt viscosity and enhance eruption explosivity for deep sea eruptions remains unknown.

Large pumice rafts are typically associated with explosive eruptions[23–27]. The 18 July 2012 eruption of the Havre submarine volcano (Kermadec Arc, NZ) went unobserved but was later recognised from a massive pumice raft (1.2 km³) through direct observation and satellite images two weeks after eruption[28,29] and was likewise initially thought to have recorded an explosive eruption[29]. However, the 2012 eruption was later concluded to be effusive[30–34] based on the discovery of many lava flows, domes, and ash produced during the eruption at the volcano summit[32,35–38] and magma ascent models based on seafloor pumice melt properties[30]. The high hydrostatic pressures that would have existed at the summit depth of 900 m below sea level are thought to hinder magmatic volatile exsolution and therefore magmatic volatile-driven fragmentation[39,40].

A new observation reported here is that in addition to the dominant white, crystal-poor pumice[41] some Havre raft pumice have a range of intensities of pink colouration (Fig. 1). The pink colour is pervasive through the pumice and demonstrably not just a surficial feature or a result of post-eruptive precipitation of hydrothermal minerals. Pink pumice has not been observed in sampled seafloor pumice deposits[30–34,42]. Notably, pink pumice has also been reported from pumice rafts of other unobserved submarine eruptions nearby at Healy (~1150 mbsl) and Raoul SW (~1200 mbsl) volcanoes in the Kermadec arc[43,44].

Here we show that the Havre pink pumice reflects high-temperature oxidation of magnetite nanolites and microlites and we interpret an explosive eruption column ejected pumice into the atmosphere at near magmatic temperatures (890 ± 27 °C[41]). Magnetic analysis, backscattered electron (BSE) imaging, transmission electron microscopy (TEM) images and X-ray fluorescence microscopy (XFM) elemental maps indicate magnetite nanolites are pervasive in the Havre white raft pumice and are oxidized to hematite in the pink raft pumice. Fe K-edge X-ray absorption near edge structure (XANES) spectroscopy shows that both magnetite and hematite are more abundant in pink pumice than in white raft pumice, and importantly that magnetite nanolites and hematite are absent from the seafloor pumice. We also show that the pink colour can be reproduced experimentally by equilibrating white Havre 2012 pumice at temperatures above ~800 °C in air within minutes, reinforcing the interpretation that the pink colouration is the result of pumice interacting with the atmosphere at near magmatic temperatures[5,8]. Our results

suggest that magnetite nanolite nucleation played an important role in initiating an explosive phase of the Havre 2012 eruption and is essential for the formation of pink pumice by providing the mineral precursor that oxidises to hematite when exposed to air.

Results and discussion

Havre 2012 pumice characterization. The 18 July 2012 Havre eruption evacuated ~1.3 km³ (bulk volume) of rhyolitic pumice, where 93 % (~1.2 km³) of the erupted pumice volume produced a pumice raft and the remaining 7% (0.1 km³) formed a deposit of giant seafloor pumice surrounding the volcanic summit[29,32]. Near-vent deposits of sunken pumice cover >35 km² of the summit caldera and pumice clasts are distinctively large, ranging in size from ~1 to 9 m in diameter[30,32,33]. The volumetrically dominant raft pumice and small-volume seafloor pumice are similar in appearance, general composition and texture, suggesting they had shared the same effusive eruptive origin[30]. Although recently it has been proposed submarine eruption models based on seafloor pumice deposits are not necessarily appropriate to estimate mass eruption rates of pumice rafts[41,45].

Havre pumice raft material began washing ashore across the SW Pacific[28,41,46] from November 2012 (Supplementary Notes 1, Supplementary Fig. S1). While the majority of the pumice comprising the raft and seafloor deposits is white to banded white/grey, a substantial proportion of the stranded raft pumice collected from Tonga and along the Eastern coast of Australia is light brown-tan to red-pink[41]. (Fig. 1a–d; Supplementary Fig. S2; colours based on the 2018 Munsell colour chart). This colour commonly occurs in highly vesicular white pumice clasts that contain coalesced vesicles (up to 1 cm diameter) where pumice clast permeability is highest.

Pumice colour can reflect magma composition and mineralogy[47,48]. Havre pumice consists of vesiculated glass, phenocrysts and microlites. All Havre pumice types have a similar mineralogy[17,21] and comprise phenocrysts of plagioclase, orthopyroxene, and magnetite with trace clinopyroxene and rare quartz[32,41] with a subtly higher proportion of phenocrysts present in the seafloor pumice (compare Fig. 1d and Fig. 1e, f)[34,41]. X-ray fluorescence elemental maps (Fig. 1e–h; Supplementary Notes 2 and Supplementary Fig. S3) and glass compositions (Supplementary Notes 3; Supplementary Table S1) reveal only subtle differences in glass composition between raft pumice and seafloor white pumice. Importantly, FeO_T ($FeO_T = FeO + Fe_2O_3$) is similar amongst white and pink raft pumice (2.39 ± 0.10 wt. % and 2.41 ± 0.06 wt. %, respectively), and seafloor white pumice (2.45 ± 0.06 wt. %)[34], ruling out elemental variations between pumice types as a cause for differences in colour.

We use the following terminology for crystal sizes: nanolites <1 µm[22], microlites for 1–30 µm, and microphenocryst 30–100 µm crystals[14,49]. Microlite mineralogy is orthopyroxene, magnetite, and plagioclase[32,34,41] and the microlite number density (MND; Supplementary Notes 4: Supplementary Table S2) is similar in the white raft pumice and white seafloor pumice (~5 × 10⁵ cm⁻²) but higher in the pink raft pumice (~1 × 10⁶ cm⁻²). Magnetite MND in the pink pumice is up to 9 times greater than in the seafloor pumice, accounting for the bulk difference in the overall MND between the pumice types.

Micron scale XFM images show discrete regions of high Fe abundance (Fig. 1i–l) in the white and pink raft pumice, which we interpret as magnetite microlites. In pink raft pumice, high resolution BSE imaging shows that magnetite is typically observed as microlites and nanolites commonly lining vesicle walls in the pink pumice consistent with where colouration is observed and concentrated (Fig. 2, see also Supplementary Notes 5 and Supplementary Fig. S4). XFM analysis also reveals magnetite is
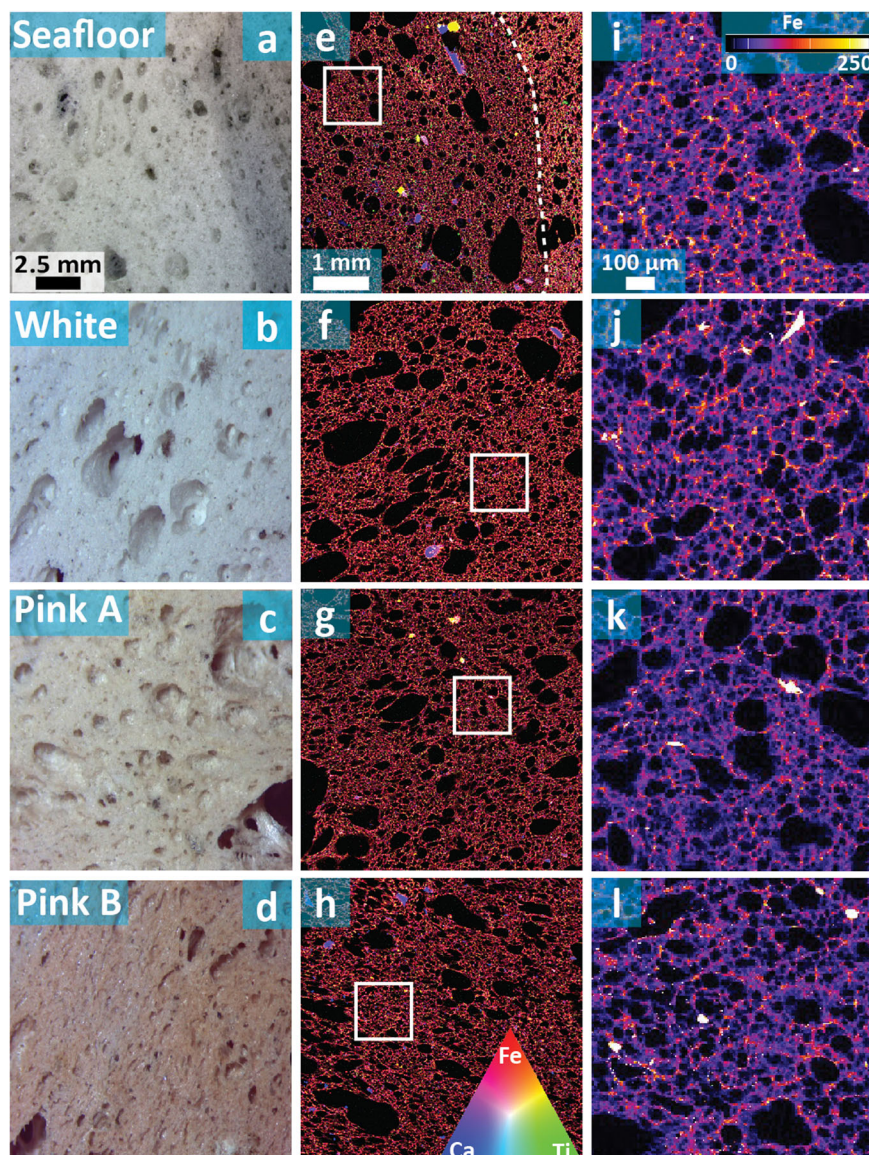
Fig. 1 Characteristics of the main pumice types from the 2012 Havre eruption. a–d Stereoscope images showing the representative colours and textures of the 4 pumice types analysed in this study; white and pink refer to pumice raft material. Note the grey and white pumice bands in the seafloor pumice. **e–h** XFM-Fe, Ti, Ca-RGB stacked elemental maps for the different pumice types. Boundary between white and grey pumice domains for the seafloor pumice indicated by white dashed line in (**e**). XFM elemental maps are colour-coded based on a RGB triangle where red, green and blue are end members correlating to high Fe, Ti and Ca, respectively. Where multiple elements are co-located, the pixel displays a colour that represents the relative proportion of each element's concentration. For example, Fe–Ti oxides will appear yellow, orthopyroxene crystals will appear pink and plagioclase crystals blue. **i–l** Corresponding XFM Fe elemental maps for the areas outlined by white boxes in (**e–h**). Fe elemental maps are set to a fire colour scale (μg*cm^{-2}) where white pixels correlate to areas of high Fe-intensity, indicating Fe–Ti oxide microlites. Yellow pixels represent either orthopyroxene microlites or Fe–Ti nanolite glass mixtures. Scale bars in top row (**a**, **e**, **i**) applies to the entire column below (e.g., **a**, **b**, **c**, **d** are in the same scale as presented in (**a**).

present in the seafloor pumice as larger microlites (Fig. 1i). and microphenocrysts (Fig. 1e).

Nanolite Identification. Nanolites can drastically affect melt rheology, and their crystallization can result in an abrupt change in melt viscosity altering eruption behaviour from effusive to explosive eruptions[13,14,16–19,22]. Nanolite identification and characterization is therefore becoming increasingly important in understanding eruption dynamics and hazard potential. To document nanolite minerology, size and relative abundances in the Havre 2012 white and pink raft and seafloor white pumice, we use a multifaceted approach of rock magnetics (i.e., magnetic hysteresis and frequency dependence of magnetic susceptibility),

transmission electron microscopy (TEM) and complementary EDS analysis of TEM imaged areas.

Magnetic hysteresis analysis provides information on the magnetite mineralogy and grain size characteristics[17,50]. Magnetic data for the white raft and seafloor pumice both indicate the presence of magnetite, whereas the pink raft pumice displays a wasp-waisted hysteresis suggesting a mixture of magnetite and hematite (Fig. 3. c, f) based on the high coercivity of hematite controlling the closure of the hysteresis loop above 0.6T[51]. The raft and seafloor pumice display thin hysteresis loops with coercivities approaching zero consistent with a superparamagnetic (SP) signature (Fig. 3a–c) which represents the presence of magnetite nanolites <20 nm[52–55]. However, the hysteresis loops are not perfectly reversible, and the magnetic remanence (M_r)
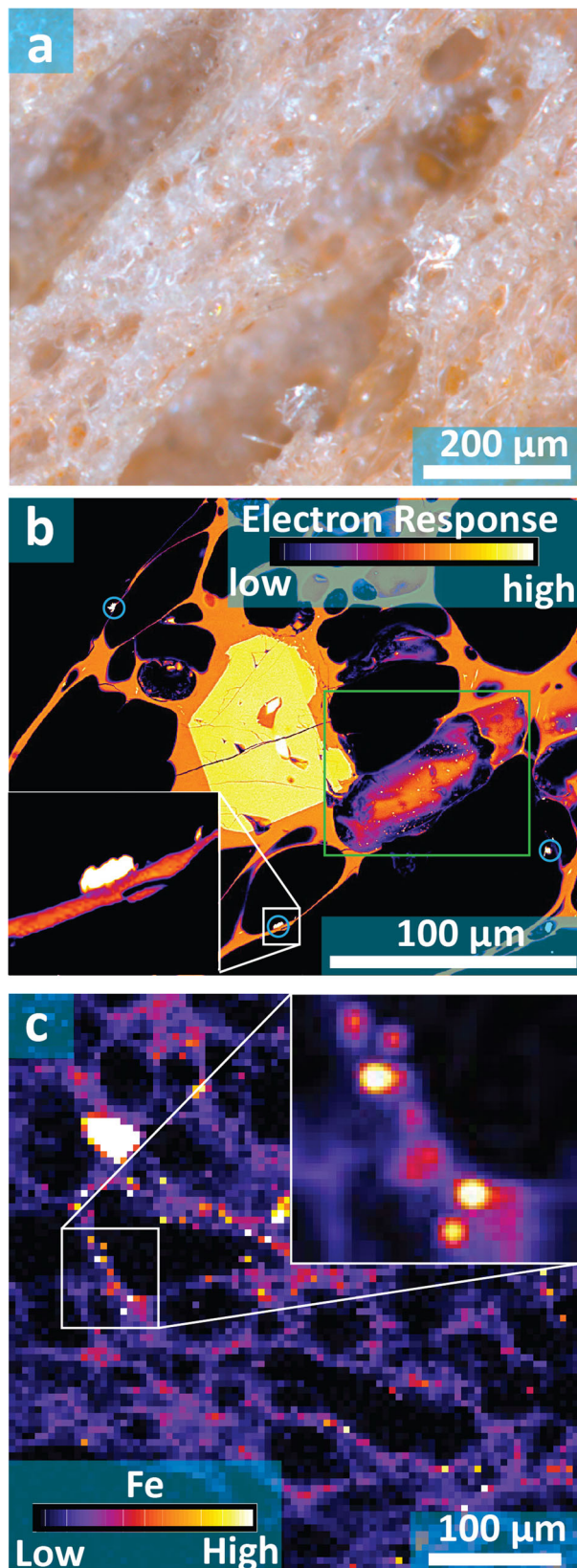
Fig. 2 Microlites and nanolites on vesicle walls in natural pink pumice. a Optical stereoscope image of natural pink pumice showing vesicle rims and walls marked by an orange-red staining. **b** BSE image showing magnetite microlites/nanolites (white) within the pumice glass (orange-yellow), where black spaces correspond to vesicles or void spaces. Note the view of the preserved concave vesicle wall (outlined by green box) that contains abundant magnetite nanolites to microlites. Blue circles highlight magnetite microlites occurring along vesicle walls. The large yellow crystal in the centre of the image is an orthopyroxene microlite. **c** An enlarged area of the XFM Fe elemental map of the pink raft pumice (Fig. 1i) showing a vesicle lined with numerous pixels with high Fe concentrations (white) interpreted to be magnetite microlites/nanolites. XFM elemental maps resolution is limited to 5 μm.

remanence/coercivity (H_{cr}/H_c) (Supplementary Table S3) can be useful measures of grain size populations in a sample visually displayed with a Dunlop (2002) plot[57] (Supplementary Notes 6; Supplementary Fig. S5). We note that a number of variables (e.g., mixing of magnetic phases, particle shape, mineral stoichiometry, internal stress, etc.) can influence the domain state interpretation in a Dunlop (2002) plot[58]. This places the high-field magnetic hysteresis data for all pumice types above the theoretical curves for MD + SP or SD + MD trends and data fall in the lower area of SD + SP mixes for SP particles <10 nm[57] (Supplementary Fig. S5). At first glance, the H_{cr}/H_c ratios (>4) for all pumice types are consistent with purely MD grains. However, the M_r/M_s ratios are too large (>0.05) in the pink raft pumice and the H_{cr}/H_c values are much too high (>10) in the white and pink raft pumice to represent purely MD grains. Although the white seafloor pumice displays a similar hysteresis shape as the white raft pumice and low M_r/M_s indicates a SP signature, the H_{cr}/H_c ratio is between 4 and 10, which is more typical of larger magnetite microphenocrysts with MD grain behaviour (>30 μm)[59].

To further investigate SP signatures relating to magnetite nanolites <20 nm in the Havre pumice suite, the frequency dependence of magnetic susceptibility (χ_{fd}) was measured over one order of magnitude frequencies (465 to 4650 Hz). The maximum theoretical χ_{fd} value for a sample with 100% SP magnetite is ~16%[60]. In the white and pink raft pumice there is a χ_{fd} of ~2.2% and 4.2%, respectively, indicating that there is an abundance of magnetite nanolites <20 nm, mixed with a component of microlites (Fig. 2). In contrast, a $\chi_{fd} = 0\%$ for the white seafloor pumice indicates the absence of nanolites, attesting to purely microlite to microphenocryst sized magnetic carriers (Fig. 1e, i), despite the similar hysteresis shape to the white raft pumice. This provides further evidence that there is increasing abundance of magnetite nanolites from the white to pink raft pumice, with no magnetite nanolites present in the seafloor pumice.

TEM imaging is utilized here to characterize the size of nanolites bound in the pumice glass. In the white and pink raft pumice we find an abundance of nanolites which are <10 nm in size (Fig. 4a, b). Nanolites are often observed in amalgamations in scanning transmission electron (STEM) images (Fig. 4c, d) consistent with high concentrations of Fe speckles in the corresponding energy dispersive spectroscopy (EDS) analysis areas (Fig. 4e, f). In comparison, no nanolites could be detected in the white seafloor pumice glass consistent with a lack of frequency dependence of magnetic susceptibility.

Magnetite and hematite in Havre 2012 pumice. The magnetics data indicate the pink colouration of the raft pumice is related to the presence of hematite. Spatially resolved Fe K-edge XANES spectra (Supplementary Notes 7; Supplementary Fig. S6) were

and coercivity (H_c) is not at zero (Fig. 3d–f), attesting to either a mixture of SP grains (i.e., magnetite nanolites <20 nm) and single domain (SD; magnetite nanolites <76 nm[56]) and/or multi domain (MD; magnetite >76 nm[56]) grains or simply the presence of MD grains alone. Magnetic hysteresis parameter ratios of magnetic remanence/magnetic saturation (M_r/M_s) and coercivity of
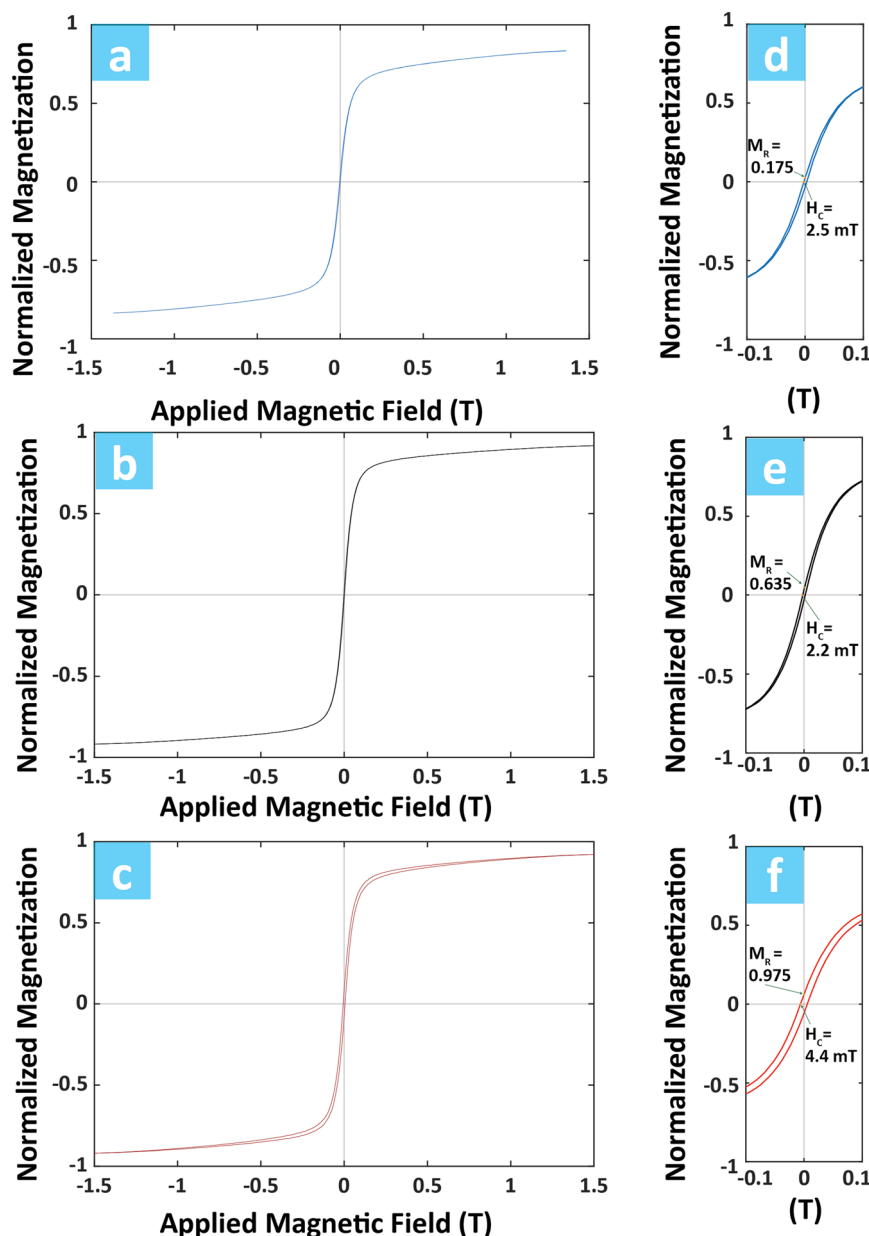
Fig. 3 Magnetic hysteresis. Magnetic hysteresis results for **a** seafloor white pumice **b** Havre white raft pumice and **c** pink raft pumice with **d**–**f** close ups of the origin of the magnetic hysteresis results highlighting subtle differences in magnetic remanence (M_R) and coercivity (H_C) between the different pumice types. A combination of magnetic parameters (Supplementary Table S3) and frequency dependence of magnetic susceptibility (χ_{fd}) are utilized to determine that the white and pink raft pumice hysteresis loops represent a mixture of superparamagnetic (SP) < 10 nm and MD magnetite grains, and that seafloor white pumice contains purely MD magnetite. In addition, **c**, **f** Havre pink raft pumice displays a classic wasp-waisted hysteresis signature closing past 0.6T suggesting that both magnetite and hematite are present[51]. Duplicates for white and pink raft pumice sample type show similar results as displayed here, while limited material of white seafloor pumice allowed for only one analysis.

recorded at the XFM beamline of the Australian Synchrotron[61] to determine the proportion and distribution of magnetite and hematite nanolites/microlites within the glass framework of a suite of Havre 2012 pumice (Fig. 3; Supplementary Fig. S7). The results, together with Fe elemental maps are presented in Fig. 5 and show that magnetite is present in the seafloor pumice while both magnetite and hematite are present in all samples of the white and pink raft pumice, with a progressive increase in the amount of magnetite and hematite from white raft pumice to pink raft pumice. Hematite is absent in the seafloor pumice. Comparison of Fe-elemental maps (Fig. 3a–f) and magnetite and hematite distributions (Fig. 5g–l) reveals that higher magnetite

and hematite proportions correspond to regions of higher Fe concentration suggesting that bright regions in the Fe maps (Fig. 5a–f, Fig. 2c) are likely to be magnetite or hematite-altered nanolites and microlites. Close inspection of the Fe maps (Fig. 5a–f) shows that these nanolites and microlites are concentrated around the vesicle rims (Fig. 2).

The Fe-XANES spectra indicate that the proportion of Fe as Fe-oxides (magnetite + hematite) in the white seafloor and some white raft pumices are small and nearly identical, with the seafloor pumice containing magnetite and the white raft pumice containing magnetite and small amounts of hematite (Fig. 5g–i, o). In contrast, pink raft pumice has considerably higher proportions of
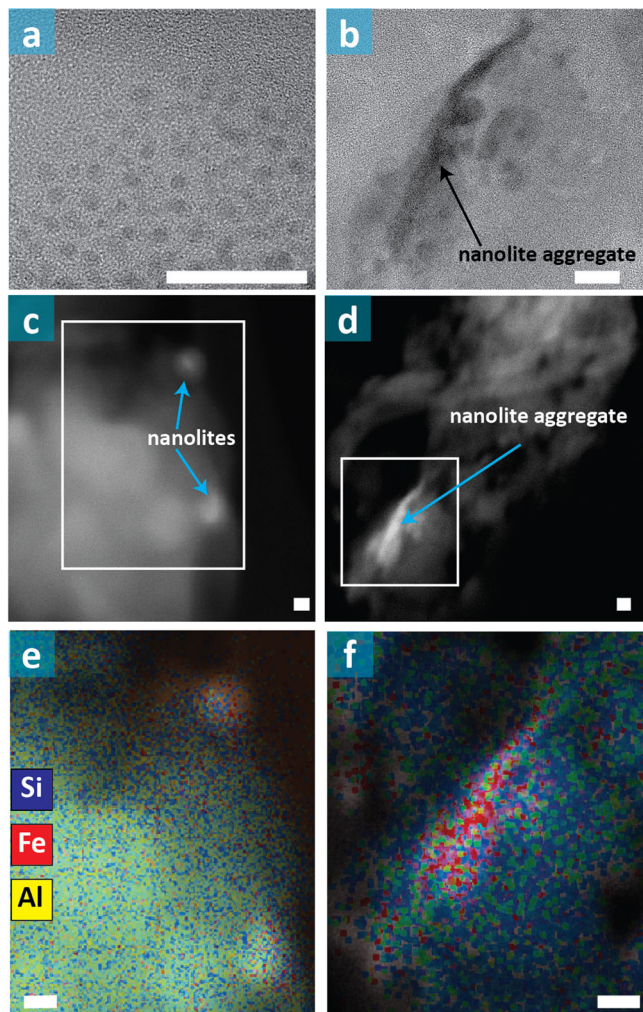
Fig. 4 Nanolite identification in the Havre 2012 pumice raft. TEM images of nanolites (darker greys) bound in the glass of the Havre 2012 for **a** white and **b** pink raft pumice. STEM micrographs of regions of **c** white and **d** pink raft pumice. EDS elemental mapping areas for **e** white and **f** pink raft pumice corresponding to the white boxes in (**c**, **d**). Fe-rich areas are depicted in red and represent magnetite and/or hematite nanolites. Glass areas are represented by blues, yellows to greens corresponding to high concentrations of Si and Al. Scale bars in all panels are equal to 20 nm.

both magnetite and hematite (Fig. 5j–l, o), in agreement with MND analysis that showed substantially more magnetite in the pink raft pumice compared to the seafloor pumice. A strong positive correlation exists between the percentage of both magnetite and hematite and the intensity of reddening in the raft pumice (Fig. 5h–l, o).

To simulate possible eruptive conditions and air interactions that might cause magnetite oxidation and pink colouration, we undertook atmospheric heating experiments (Supplementary Notes 8). White raft pumice was heated to temperatures between 675 and 900 °C for 2.5–25 min under atmospheric conditions (Supplementary Fig. S8). No colour change occurred at 675 °C, while the orange-pink to pink-red colour observed in natural Havre raft pumice was produced near magmatic temperatures[41] of 800 and 900 °C within 2.5–10 min (Supplementary Fig. S8c, d, S9a–d). The speckled pink to red staining (Supplementary Fig. 8d) implies the colour change is due to magnetite microlites and nanolites oxidizing to hematite[8,18,62]. The experimental samples with more abundant larger vesicles that display a greater degree of interconnectivity developed more intense and penetrative colouration (Supplementary Fig. S10).

Tait et al.[8] hypothesized subaerial pink pumice forms from high-temperature oxidation of Fe stored either within the pumice glass or magnetite microlites. Our analyses indicate that high-temperature oxidation of magnetite nanolites and microlites to hematite is the primary mechanism for the development of pink colouration. Furthermore, the results suggest a substantial proportion of magnetite microlites and nanolites need to be available to oxidize to hematite for a visible pink colouration to develop. Some white raft pumice does not have sufficient hematite to become visibly pink. We hypothesize that this is due to insufficient time spent in the air at high temperatures to convert the available magnetite to hematite. The required time is likely dependent on the amount of precursor magnetite available in the pumice glass and clast permeability to allow oxygen penetration and interaction with the nanolites.

Evidence for a short-lived explosive phase of the Havre 2012 eruption. We have shown that pink pumice forms when hot, magnetite microlite and nanolite bearing pumice is exposed to air allowing magnetite to oxidise to hematite in sufficient quantities to be macroscopically visible (Fig. 2a). Magnetite and hematite are present in all raft pumice with increasing amounts of both minerals from the white raft to pink raft pumice (Fig. 5). Neither pink colouration nor hematite are present in the Havre seafloor pumice investigated here, consistent with previous studies that concluded that the Havre seafloor pumice did not interact with the atmosphere[30,31,34]. The results of our heating experiments (Fig. S8) support the existing evidence that for high-temperature Fe-oxidation to occur, clasts need to remain at high temperatures (>700 °C) for several minutes in the air[8,62,63].

The effusive phases of the Havre 2012 eruption produced large pumice clasts which could buoyantly rise to the ocean surface from the 900 mbsl; a 9 m sized clast with 90 % vesicularity could ascend in as little as 63 s[30]. Clasts with decreasing size and vesicularity will have increasing ascent times to the ocean surface; clasts <1 m become waterlogged and sink before reaching the surface[30]. This ascent time could allow the core of a large clast to retain some of its original magmatic entropy[64]. As pumice floats in, rather than on the water[26], pumice that breaks up at the surface due to quench fragmentation will be immediately quenched by seawater[64]. Explosions of the large pumice clast at the ocean surface would therefore be required to eject fragments of initially shielded hot interiors into the air. A key requirement to generate pink pumice is hot pumice to remain airborne for several minutes, which is equivalent to reaching approximately 2 km above sea level[8,65]. Ocean surface explosivity has only been observed to ballistically eject fragments to heights of a few hundred meters[66,67] which does not allow sufficient time to become visually oxidized and form pink pumice. Therefore, any pumice clasts buoyantly rising through the ocean column and exposed to the atmosphere by secondary fragmentation and breakup at the ocean surface cannot be oxidized to form the pink raft or white raft pumice. Furthermore, such a mechanism would only result in a small proportion of the volumetrically dominant raft pumice becoming oxidized. All analysed white and pink raft pumice has been oxidized and contains hematite, indicating the majority of the volumetrically dominant pumice raft is comprised of oxidized material. Importantly then, the mechanism for delivering hot pumice to the surface needs to be capable of delivering the bulk of the pumice raft volume at near magmatic temperatures to the atmosphere where it can remain for several minutes before being deposited on the ocean surface.
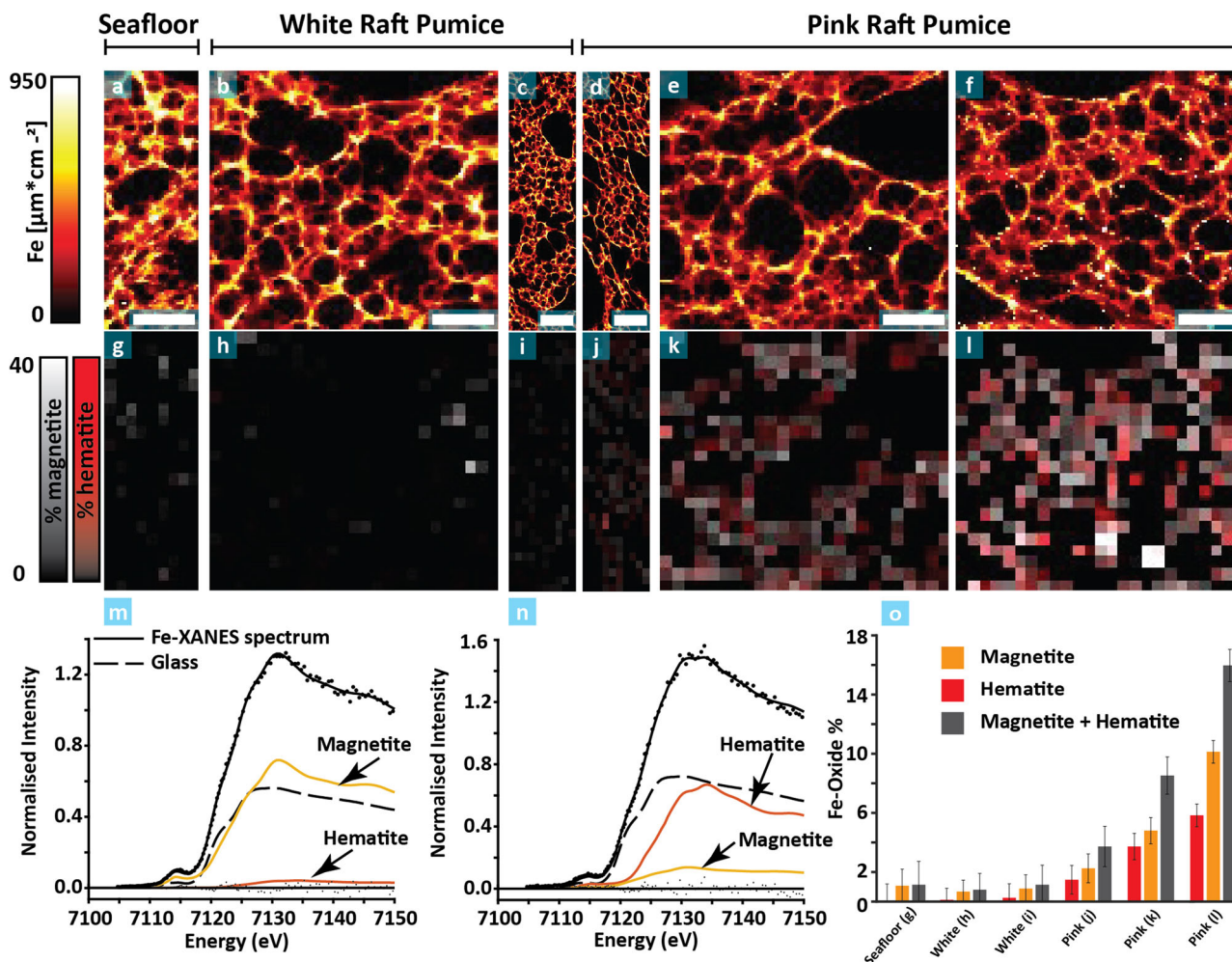
Fig. 5 Fe-XANES maps of the Havre 2012 pumice suite. a–f XFM Fe elemental maps ($\mu g \ast cm^{-2}$) where white pixels correspond to areas of high Fe-intensity, indicating magnetite microlites and nanolites. White scale bars are all equal to 100 μm and scale bars correspond to the panel below each column (e.g., the scale bar in (**a**) corresponds to the scale bar in (**g**)). **g–l** Corresponding Fe-XANES maps presenting the proportion of magnetite (grey scale) and hematite (red scale) merged into one image. **m**, **n** Example Fe-XANES spectra of individual pixels results of linear least squares combination fitting (black solid line) with high proportions of **m** magnetite and **n** hematite from within the pink raft pumice Fe-XANES area in 3l. Here we show the spectral contributions from magnetite (yellow solid line), hematite (red solid line), and glass (dashed black line) which combined equal the sum-spectrum data (filled black circles). Residuals in the fit (black dots) are shown with a line at zero intensity to guide the eye. Additional spectra from all samples are shown in Supplementary Fig. S8. **o** Percentage of Fe as hematite (red) and magnetite (yellow) in each Fe-XANES analysis area. Percentages are calculated by averaging the portion of magnetite and hematite in every pixel of an Fe-XANES area determined by fitting every pixel as shown in (**m**). The error was calculated as the mean of the normalized sum of the residuals from the linear combination fitting. Samples: **a**, **g** white seafloor pumice (same as in Fig.1a, e), **b**, **c**, **h**, **i** two different white raft pumice samples (**b**, **c** are the same white pumice in Fig. 1a, e), **d–f**, **j–l**) 3 pink raft pumice samples with different intensities of colouration: **d**, **j** tan-brown, **e**, **k** orange-pink (Fig. 1c, g), **f**, **l** red-pink pumice (Fig. 1d, h).

We propose that an unrecognized explosive phase of the Havre 2012 eruption is required to achieve the conditions necessary to oxidise magnetite to hematite in all raft pumice and generate the pink pumice. We envision a short-lived explosive eruption column breaching the ocean surface that would allow hot pumice to directly interact with the oxygen-rich lower atmosphere (Fig. 6), become air-filled and initiate high-temperature oxidation of magnetite nanolites to microlites in the pumice glass (Fig. 5).

Havre rhyolite magma was primed for volatile saturation and vesiculation on eruption[41]. Magnetite crystallization was likely promoted by degassing and/or undercooling in response to initial decompression[17,20,22,68,69] (Fig. 6b). Continued decompression would explain the observed range in size of magnetite nanolites (Fig. 4) and microlites, where initial nanolites would have grown in size[70] to form magnetite microlites in the raft pumice (Fig. 1k–l, Fig. 2). Once formed, the magnetite nanolites and

microlites would collectively have resulted in a near instantaneous increase in melt viscosity, causing gas bubbles to become isolated in the stiffened melt[18]. Nanolites act as sites for enhanced exsolution of volatiles indicated by coalesced vesicles lined with nanolites and microlites in the raft pumice (Fig. 2)[12–14,17]. Through this process, trapped gas would have rapidly expanded on further decompression thereby initiating brittle fragmentation and a violent explosive eruption. The magnetite crystals then provide ample sites for oxidation once exposed to the atmosphere following rapid transfer in the penetrative explosive eruption column. In this model, pink pumice would correspond to the rapidly ascending core of the eruption column (Fig. 6b; dashed lines). A steam and gas-rich plume would provide extra protection from water interaction and cooling of the eruption column core, allowing the central parts of the submarine eruption column to potentially behave similarly to a subaerial
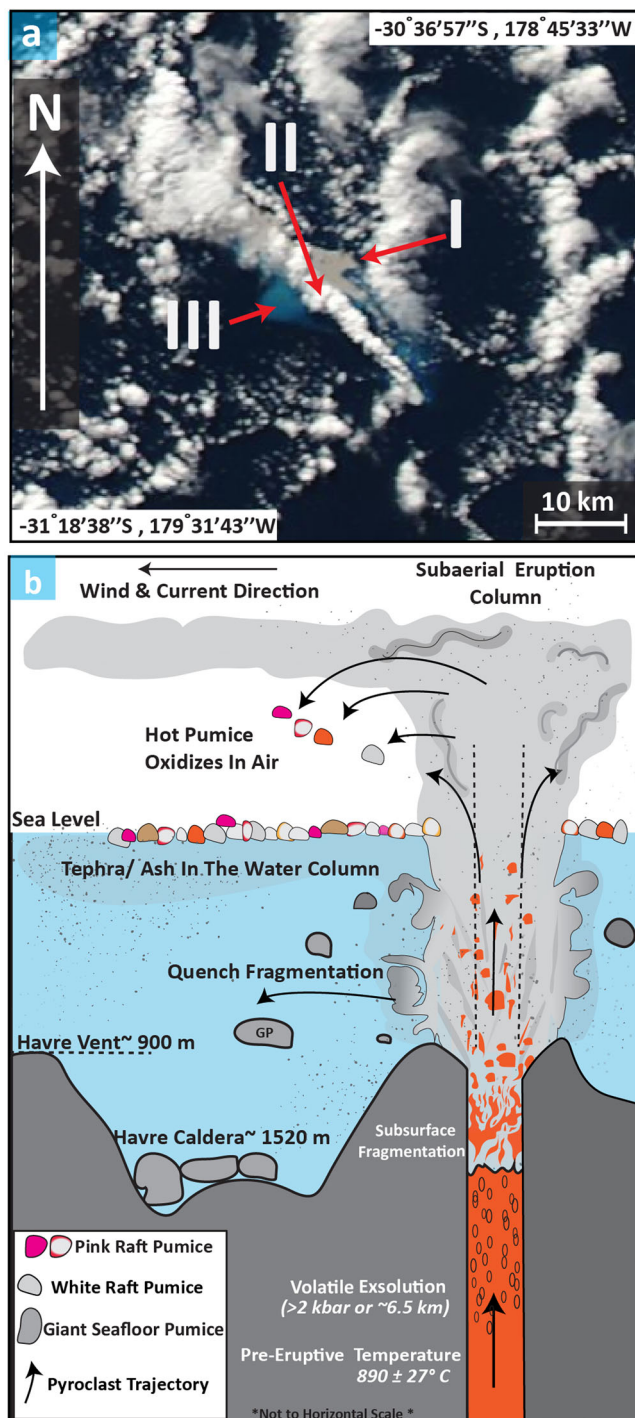
Fig. 6 2012 Havre explosive eruption model. a NASA Aqua Modis (Moderate-resolution imaging Spectroradiometer) satellite true colour image ~21 h after eruption onset (01:26 UTC July 18, 2012) showing the pumice raft (I) that had covered an area of ~400 km². [28,29], a gas/steam vapour plume (II) extending ~50 km downwind, and suspended ash/tephra at shallow water depths (III) surrounding the pumice raft. **b** Eruption model showing an explosive eruption column triggered by exsolution of volatiles at depth, leading to subsurface magmatic volatile-driven fragmentation. Black arrows represent trajectories of pumice types examined in this study assuming the raft and giant seafloor pumice (GP) were erupted contemporaneously. The explosive eruption column punctures the overlying ocean water column allowing pumice to enter the atmosphere at near magmatic temperature[33] where it can then undergo oxidation. The white and pink raft pumice are erupted through the centre of the eruption column, where decompression rates were highest promoting syn-eruptive growth of magnetite nanolite and microlite crystals. While all pumice ejected into the atmosphere to form the pumice raft likely undergoes some Fe-oxidation, physical characteristics (i.e., clast permeability[5], temperature & magnetite abundance) and residence time in atmosphere are limiting factors on Fe-oxidation occurring and pink colouration developing. Substantial non-explosive to explosive water-magma interaction along column margins (refs. [38,71,73]) is also expected, quickly cooling and waterlogging pumice and quenching giant seafloor pumice precluding any high temperature oxidation of magnetite to hematite. Eruption model not to horizontal scale. We acknowledge the use of imagery from the NASA Worldview application (https://worldview.earthdata.nasa.gov/), part of the NASA Earth Observing System Data and Information System (EOSDIS).

model puts in to question the relationship between the giant seafloor pumice and the pumice raft[13]. The larger magnetite microlite to microphenocryst size and lack of obvious magnetite nanolites (Fig. 1e)[33,34] suggest the seafloor pumice experienced more protracted syn-eruptive crystallization during slower ascent, and therefore, different trajectories on eruption. The lack of hematite in the seafloor pumice (Fig. 5g, o) precludes any high-temperature atmospheric oxidation. If the seafloor pumice is temporally related to the explosive eruptive phase that produced the pumice raft then we suggest that the seafloor pumice represents magma from the margins of the conduit and eruptive column[34]. Erupted material along the column margins would interact extensively with seawater enhancing cooling and promoting sinking[30,37,38,71,73]. Consequently, pumice in submarine explosive eruptions can either be air-cooled and therefore buoyant and float to form rafts[26,27], or water-cooled and sink to the seafloor near the vent[30,42]. At Havre, this duality is produced by the respective locations of pumice material in the eruption column and resultant trajectories that lead to air cooling of the raft and water cooling of the seafloor pumice.

Our interpretation that the pumice raft of the 2012 Havre eruption originated from a magmatic volatile-driven explosive eruption challenges theoretical models[39,40] of the limiting depth of magmatic volatile-driven fragmentation in the marine realm. Others have shown the importance of magnetite nanolites that form upon decompression in changing the rheology of the melt and providing conditions needed for catastrophic explosive eruptions[17–19]. Future studies related to nanolite nucleation would benefit by constraining the rates of nanolite nucleation, the quantity of nanolites needed to shift viscosity over fragmentation thresholds and the rate of volatile exsolution in response to nanolite nucleation for varying melt compositions. Recent modelling of gas jet thrusts in submarine eruptions suggest there is some depth limitation (<1000 m) for an eruption to breach the surface[74]. However, such models could be expanded on to incorporate the effect of nanolite crystallization and the

eruption[34,71,72]. Differences in the proportion of magnetite microlites in the pumice raft is likely due to variable decompression rates in the volcanic conduit, resulting in lower magnetite microlite proportions in the white raft pumice. These variable decompression histories would place white raft pumice as material that is marginal in relation to the core of the explosive eruption column.

It is clear that the Havre eruption had many effusive eruptive phases to produce the multiple summit lava flows and domes[31,32,35]. Our results and analysis, however, suggest that the pink raft pumice is a visual marker recording a violent but short-lived explosive phase to the eruption, which generated an eruption column that breached the ocean surface. This eruption

consequent effects on spontaneous enhanced melt viscosity and volatile exsolution has on explosivity at varying pressures and therefore water depths. This highlights the need for further investigation into nanolite occurrence and their influence on submarine eruption behaviour, particularly as it applies to eruptions which form large and hazardous pumice rafts. We have shown that high-temperature Fe-oxidation of magnetite nanolites to hematite results in the formation of pink pumice upon air interaction. As it is rare to observe these deep-sea eruptions, re-examining pink pumice reported from other deep-sea submarine eruptions[43,44], such as Healy (~1150 mbsl) and SW Raoul (~1200 mbsl) would be useful tests of the eruptive model proposed here. We conclude that pink pumice in pumice rafts is a valuable visual key for the detection of unrecognized atmosphere-penetrating explosive eruptions from submarine volcanoes.

Methods

Sample collection and preparation. Samples were collected from stranded pumice raft material deposited mainly on the eastern shores of Australia as outlined in Supplementary Materials (Fig. S1). Pumice samples for most micro analysis (i.e., BSE, XFM, Fe-XANES) were embedded in epoxy, sectioned, glued to a 1 mm thick fused pure quartz glass slide and then polished to 30 μm thickness.

Electron probe microanalysis (EPMA). Glass composition is quantified by electron probe microanalysis (EPMA) following the methods reported in Knafelc et al.[41] (Supplementary Table S1) and is further discussed in Supplementary materials. Analyses by EPMA were conducted on samples embedded in 1-inch epoxy resin mounts to assure coloured domains for analysis correlate to either white or pink pumice.

X-ray fluorescence microscopy (XFM). The prepared samples were placed in the 2.5 μm FWHM focus of a 18.5 keV X-ray beam from a double-crystal Si (111) monochromator and focused with a Kirkpatrick-Baez mirror pair at the XFM beamline of the Australian Synchrotron[75]. Large areas (5 mm × 5 mm) were mapped with 1 ms dwell per 5 μm pixel with excited fluorescent photons collected with a 384 element Maia detector system[76] placed in its usual backscatter position. Spectra were analysed using the Dynamic Analysis method as implemented in GeoPIXE[77] and quantified through measurements of an Fe foil (Micromatter, Canada). Individual elemental maps were exported as quantitative 32-bit tiff files for further analysis (Supplementary Notes 4; Supplementary Fig. S3).

Backscattered electron microscopy. BSE maps of 500 μm × 500 μm areas of slides from which Fe-XANES spectra were recorded (Fig. 3h, l) were acquired using a TESCAN MIRA3 scanning electron microscope (SEM). BSE maps were produced using an accelerating voltage of 15 kV and a beam current of 720 pA (beam intensity setting 13, spot size 11 nm) at a working distance of 15 mm, and stitching images with a FOV = 256 μm (Fig. S4). Microlite number densities (MND) were calculated using grey scale analysis in ImageJ software[78] of BSE images with FOVs of 276.8 μm (×1000 magnification) and 553.6 μm (×500 magnification) and details are further outlined in the Supplementary materials (Supplementary Table S2).

Rock magnetics. Magnetic hysteresis measurements were conducted following the method of Knafelc et al.[79] Here, a set of raft (i.e., white, and pink) and seafloor pumice samples were analysed five times and averaged to reduce the noise of the resulting hysteresis loops. The samples were prepared into ~1 mm thick cylinder wafers to reduce the influence of phenocrysts (3–5% modal abundance) on magnetic glass analysis. Normalization to the highest magnetization and a 70% high field slope correction were applied to each hysteresis loop. Frequency dependence of magnetic susceptibility (χ_{fd}) was measured using a Bartington MS2B sensor over two orders of magnitude frequency (465–4650 Hz). Magnetic susceptibility was measured 10 times at each frequency for the raft pumice samples and 20 times for a white seafloor pumice sample.

Transmission electron microscopy (TEM). Transmission electron microscopy (TEM) images were acquired using a JEOL 2100 operated at 200 kV mounted with a TVIPS F416 4K CCD camera (Fig. 4). EDS analysis of TEM image areas was performed with an Oxford X-Max high-sensitivity silicon drift X-ray detector. Powdered samples were treated with a magnet to remove loose magnetic material prior to mounting. Treated powder was sonicated for 5 min in 100% EtOH and drop cast onto 300 mesh lacey carbon copper grids and left to air dry. Once dry, samples were plasma cleaned using an Evactron Plasma Cleaner prior to imaging.

Fe K-Edge X-ray absorption near edge structure (Fe-XANES). Regions of interest (500 μm × 500 μm) were selected from the XFM elemental maps for the acquisition of Fe K-Edge X-ray absorption near edge structure (Fe-XANES) spectra. The fluorescence intensity was recorded at 220 non-uniformly spaced incident energies from 6963 eV to 7463 eV with 2 ms dwell per 4 μm pixel for all samples except Fig. 3i, j, which had a dwell of 0.8 ms per 4 μm pixel using the experimental geometry described above for XFM analysis. Intensity maps for each incident X-ray energy were generated and exported as described above for elemental maps. The intensity maps at each energy were binned to achieve a constant per pixel dwell of 50 ms per pixel to increase the signal to noise ratio yielding a final pixel size of 20 μm for all regions except Fig. 3i, j, which achieved a final pixel size of 50 μm. The energy was calibrated to an Fe foil first derivative peak of 7112.0 eV in transmission mode, before the spectra at each binned pixel were background subtracted and normalised to an edge step of one by subtracting a linear fit to regions below the edge (7021.5 eV to 7081.5 eV) and subtracting a second linear fit to regions above the edge (E > 7200 eV). The spectra binned to a single pixel and normalised as described previously are shown in Supplementary Fig. S6 and show differences in both the peak and pre-edge shapes, together with minor differences in the edge energy. A spatially resolved linear combination analysis (Matlab® lsqnonneg) was applied to pixels where the Fe concentration was above the noise level to identify regions containing hematite and magnetite (Fig. 3m, n; Supplementary Fig. S7) from regions dominated by glass using hematite and magnetite reference spectra[80] and a glass rich rhyolitic pumice spectrum from an area of white raft pumice (Supplementary Table S1) void of visible microlites and nanolites. Pixels where the linear combination analysis yielded poor results were excluded from the analysis. Less than 2% of the pixels were excluded. The magnetite and hematite maps were normalized to the amount of Fe present in each pixel and the mean of the normalized magnetite and hematite presented in Fig. 3o. The error was calculated as the mean of the normalized sum of the residuals from the linear combination fitting. Area presented for Fe-XANES analysis were exported as quantitative 32-bit tiff files for further analysis and presentation.

High-temperature oxidation experiments. High-temperature oxidation experiments were conducted on separate pieces of Havre 2012 white raft pumice clasts between 675 and 900 °C for a series of times ranging from 2.5 to 25 min in atmospheric conditions. Most experiments were conducted on white raft pumice reported here, but seafloor pumice was also used. Samples were cleaned thoroughly using a desalination method[41] before the experiments. Each sample was placed into a pre-heated *Carbolite 1 bar furnace* set to temperature. An inevitable rush of atmospheric air enters the furnace that cools the furnace 20–30 °C initially, but the furnace heats back to the specified temperature in 1–2 min. Samples were removed from the furnace and cooled in air after the specified time. Air cooling effectively cools the samples below 600 °C in seconds to tens of seconds. Samples used in the experiments ranged in size from 5 to 10 cm and there was no clear indication that the reaction is prohibited or enhanced by the size of the sample.

Data availability

The data used to produce the results of this article can be accessed through Cloudstor at the following link (https://cloudstor.aarnet.edu.au/plus/s/wVeA0yCE3vetH6x).

References

1. Browne, B. & Szramek, L. in *The Encyclopedia of Volcanoes* 203–214 (Elsevier, 2015).
2. Cassidy, M., Manga, M., Cashman, K. & Bachmann, O. Controls on explosive-effusive volcanic eruption styles. *Nat. Commun.* **9**, 1–16 (2018).
3. Humphreys, M. C., Menand, T., Blundy, J. D. & Klimm, K. Magma ascent rates in explosive eruptions: Constraints from H2O diffusion in melt inclusions. *Earth Planet. Sci. Lett.* **270**, 25–40 (2008).
4. Ersoy, O., Aydar, E., Şen, E. & Gourgaud, A. Contrasting fragmentation and transportation dynamics during the emplacement of Dikkartın rhyodacitic dome; Erciyes stratovolcano, central Turkey. *Mediterr. Geosci. Rev.* **1**, 223–242 (2019).
5. Moriizumi, M., Nakashima, S., Okumura, S. & Yamanoi, Y. Color-change processes of a plinian pumice and experimental constraints of color-change kinetics in air of an obsidian. *Bull. Volcanol.* **71**, 1–13 (2008).
6. Calder, E., Sparks, R. & Gardeweg, M. Erosion, transport and segregation of pumice and lithic clasts in pyroclastic flows inferred from ignimbrite at Lascar Volcano, Chile. *J. Volcanol. Geotherm. Res.* **104**, 201–235 (2000).
7. Christiansen, R. L., Calvert, A. T. & Grove, T. L. Geologic field-trip guide to Mount Shasta volcano, northern California. Report No. 2328-0328, (US Geological Survey, 2017).

8. Tait, S., Thomas, R., Gardner, J. & Jaupart, C. Constraints on cooling rates and permeabilities of pumice in an explosive eruption jet from colour and magnetic mineralogy. *J. Volcanol. Geotherm. Res.* **86**, 79–91 (1998).

9. Stevenson, R., Briggs, R. & Hodder, A. Physical volcanology and emplacement history of the Ben Lomond rhyolite lava flow, Taupo Volcanic Centre, New Zealand. *New Zealand J. Geol. Geophy.* **37**, 345–358 (1994).

10. Stevenson, R. J., Dingwell, D. B., Bagdassarov, N. S. & Manley, C. R. Measurement and implication of" effective" viscosity for rhyolite flow emplacement. *Bull. Volcanol.* **63**, 227–237 (2001).

11. Cooper, R. F., Fanselow, J. B. & Poker, D. B. The mechanism of oxidation of a basaltic glass: chemical diffusion of network-modifying cations. *Geochim. Cosmochim. Acta* **60**, 3253–3265 (1996).

12. Barone, G. et al. Nanoscale surface modification of Mt. Etna volcanic ashes. *Geochim. Cosmochim. Acta* **174**, 70–84 (2016).

13. Mujin, M. & Nakamura, M. A nanolite record of eruption style transition. *Geology* **42**, 611–614 (2014).

14. Mujin, M., Nakamura, M. & Miyake, A. Eruption style and crystal size distributions: Crystallization of groundmass nanolites in the 2011 Shinmoedake eruption. *Am. Min.* **102**, 2367–2380 (2017).

15. Hajimirza, S., Gonnermann, H. M. & Gardner, J. E. Reconciling bubble nucleation in explosive eruptions with geospeedometers. *Nat. commun.* **12**, 1–8 (2021).

16. Di Genova, D., Zandona, A. & Deubener, J. Unravelling the effect of nano-heterogeneity on the viscosity of silicate melts: Implications for glass manufacturing and volcanic eruptions. *J. Non Cryst. Solids* **545**, 120248 (2020).

17. Di Genova, D. et al. A compositional tipping point governing the mobilization and eruption style of rhyolitic magma. *Nature* **552**, 235–238 (2017).

18. Di Genova, D. et al. In situ observation of nanolite growth in volcanic melt: A driving force for explosive eruptions. *Sci. Adv.* **6**, eabb0413 (2020).

19. Cáceres, F. et al. Can nanolites enhance eruption explosivity? *Geology* **48**, 997–1001 (2020).

20. Cáceres, F. et al. From melt to crystals: the effects of cooling on FeTi oxide nanolites crystallisation and melt polymerisation at oxidising conditions. *Chem. Geology* **563**, 120057 (2021).

21. Burgess, K. D., Stroud, R. M., Dyar, M. D. & McCanta, M. C. Submicrometer-scale spatial heterogeneity in silicate glasses using aberration-corrected scanning transmission electron microscopy. *Am. Min.* **101**, 2677–2688 (2016).

22. Di Genova, D., Caracciolo, A. & Kolzenburg, S. Measuring the degree of "nanotilization" of volcanic glasses: Understanding syn-eruptive processes recorded in melt inclusions. *Lithos* **318-319**, 209–218 (2018).

23. Gass, I. G., Harris, P. G. & Holdgate, M. W. Pumice eruption in the area of the South Sandwich Islands. *Geol. Mag.* **100**, 321–330 (2009).

24. Simkin, T. & Fiske, R. S. KRAKATAU 1883: a centennial retrospective on the eruption and its atmospheric effects. *Weatherwise* **36**, 244–254 (1983).

25. Risso, C., Scasso, R. A. & Aparicio, A. Presence of large pumice blocks on Tierra del Fuego and South Shetland Islands shorelines, from 1962 South Sandwich Islands eruption. *Marine Geol.* **186**, 413–422 (2002).

26. Bryan, S. E. et al. Pumice rafting and faunal dispersion during 2001–2002 in the Southwest Pacific: record of a dacitic submarine explosive eruption from Tonga. *Earth Planet. Sci. Lett.* **227**, 135–154 (2004).

27. Bryan, S. E. et al. Rapid, long-distance dispersal by pumice rafting. *PLoS One* **7**, e40583 (2012).

28. Jutzeler, M. et al. On the fate of pumice rafts formed during the 2012 Havre submarine eruption. *Nat. Commun.* **5**, 3660 (2014).

29. Carey, R. J., Wysoczanski, R., Wunderman, R., & Jutzeler, M. Discovery of the Largest Historic Silicic Submarine Eruption. *Eos, Transactions, American Geophysical Union* **95**, 157–159 (2014).

30. Manga, M. et al. The pumice raft-forming 2012 Havre submarine eruption was effusive. *Earth Planet. Sci. Lett.* **489**, 49–58 (2018).

31. Manga, M., Mitchell, S. J., Degruyter, W. & Carey, R. J. Transition of eruptive style: Pumice raft to dome-forming eruption at the Havre submarine volcano, southwest Pacific Ocean. *Geology* **46**, 1075–1078 (2018).

32. Carey, R. et al. The largest deep-ocean silicic volcanic eruption of the past century. *Sci. Adv.* **4**, e1701121 (2018).

33. Mitchell, S. J., McIntosh, I. M., Houghton, B. F., Carey, R. J. & Shea, T. Dynamics of a powerful deep submarine eruption recorded in H2O contents and speciation in rhyolitic glass: The 2012 Havre eruption. *Earth Planet. Sci. Lett.* **494**, 135–147 (2018).

34. Mitchell, S. J. et al. Submarine giant pumice: a window into the shallow conduit dynamics of a recent silicic eruption. *Bull. Volcanol.* **81**, https://doi.org/10.1007/s00445-019-1298-5 (2019).

35. Ikegami, F. et al. The eruption of submarine rhyolite lavas and domes in the deep ocean—Havre 2012, Kermadec Arc. *Front. Earth Sci.* **6**, https://doi.org/10.3389/feart.2018.00147 (2018).

36. Murch, A. P. et al. Volcaniclastic dispersal during submarine lava effusion: the 2012 eruption of Havre Volcano, Kermadec Arc, New Zealand. *Front. Earth Sci.* **8**, 237 (2020).

37. Murch, A. P., White, J. D. L. & Carey, R. J. Unusual fluidal behavior of a silicic magma during fragmentation in a deep subaqueous eruption, Havre volcano, southwestern Pacific Ocean. *Geology* **47**, 487–490 (2019).

38. Murch, A. P., White, J. D. L. & Carey, R. J. Characteristics and deposit stratigraphy of submarine-erupted silicic Ash, Havre volcano, Kermadec Arc, New Zealand. *Front. Earth Sci.* **7**, https://doi.org/10.3389/feart.2019.00001 (2019).

39. Fisher, R. V. & Schmincke, H.-U. *Pyroclastic Rocks*. (Springer Science & Business Media, 2012).

40. Cas, R. A. F. & Simmons, J. M. Why deep-water eruptions are so different from subaerial eruptions. *Front. Earth Sci.* **6**, https://doi.org/10.3389/feart.2018.00198 (2018).

41. Knafelc, J., Bryan, S. E., Gust, D. & Cathey, H. E. Defining pre-eruptive conditions of the Havre 2012 submarine rhyolite eruption using crystal archives. *Front. Earth Sci.* **8**, https://doi.org/10.3389/feart.2020.00310 (2020).

42. Fauria, K. E., Manga, M. & Wei, Z. Trapped bubbles keep pumice afloat and gas diffusion makes pumice sink. *Earth Planet. Sci. Lett.* **460**, 50–59 (2017).

43. Barker, S. J., Rotella, M. D., Wilson, C. J. N., Wright, I. C. & Wysoczanski, R. J. Contrasting pyroclast density spectra from subaerial and submarine silicic eruptions in the Kermadec arc: implications for eruption processes and dredge sampling. *Bull. Volcanol.* **74**, 1425–1443 (2012).

44. Rotella, M. D. et al. Dynamics of deep submarine silicic explosive eruptions in the Kermadec arc, as reflected in pumice vesicularity textures. *J. Volcanol. Geothermal Res.* **301**, 314–332 (2015).

45. Mitchell, S. J., Fauria, K. E., Houghton, B. F. & Carey, R. J. Sink or float: microtextural controls on the fate of pumice deposition during the 2012 submarine Havre eruption. *Bull. Volcanol.* **83**, 1–20 (2021).

46. Velasquez, E. et al. Age and area predict patterns of species richness in pumice rafts contingent on oceanic climatic zone encountered. *Ecol. Evol.* **8**, 5034–5046 (2018).

47. Schlinger, C. M., Smith, R. M. & Veblen, D. R. Geologic origin of magnetic volcanic glasses in the KBS tuff. *Geology* **14**, 959–962 (1986).

48. Paulick, H. & Franz, G. The color of pumice: case study on a trachytic fall deposit, Meidob volcanic field, Sudan. *Bull. Volcanol.* **59**, 171–185 (1997).

49. Zellmer, G. F. Gaining acuity on crystal terminology in volcanic rocks. *Bull. Volcanol.* **83**, 1–8 (2021).

50. Pawse, A., Beske-Diehl, S. & Marshall, S. Use of magnetic hysteresis properties and electron spin resonance spectroscopy for the identification of volcanic ash: a preliminary study. *Geophys. J. Int.* **132**, 712–720 (1998).

51. Roberts, A. P., Cui, Y. & Verosub, K. L. Wasp-waisted hysteresis loops: Mineral magnetic characteristics and discrimination of components in mixed magnetic systems. *J. Geophys. Res. Solid Earth* **100**, 17909–17924 (1995).

52. Moskowitz, B. M. in *Environmental Magnetism Workshop (IRM)*. 48 (Inst. for Rock Magnetism Univ. of Minn., Minneapolis, Minn).

53. Tauxe, L., Mullender, T. & Pick, T. Potbellies, wasp-waists, and superparamagnetism in magnetic hysteresis. *J. Geophys. Res.: Solid Earth* **101**, 571–583 (1996).

54. Pick, T. & Tauxe, L. Characteristics of magnetite in submarine basaltic glass. *Geophys. J. Int.* **119**, 116–128 (1994).

55. Li, Q. et al. Correlation between particle size/domain structure and magnetic properties of highly crystalline Fe 3 O 4 nanoparticles. *Sci. Rep.* **7**, 1–7 (2017).

56. Dunlop, D. J. The rock magnetism of fine particles. *Phys. Earth Planet. Inter.* **26**, 1–26 (1981).

57. Dunlop, D. J. Theory and application of the Day plot (Mrs/Ms versus Hcr/Hc) 1. Theoretical curves and tests using titanomagnetite data. *J. Geophys. Re.: Solid Earth* **107**, EPM 4-1-EPM 4-22 (2002).

58. Roberts, A. P., Tauxe, L., Heslop, D., Zhao, X. & Jiang, Z. A critical appraisal of the "Day" diagram. *J. Geophys. Res.: Solid Earth* **123**, 2618–2644 (2018).

59. Pike, C. R., Roberts, A. P., Dekkers, M. J. & Verosub, K. L. An investigation of multi-domain hysteresis mechanisms using FORC diagrams. *Phys. Earth Planet. Inter.* **126**, 11–25 (2001).

60. Worm, H.-U. On the superparamagnetic—stable single domain transition for magnetite, and frequency dependence of susceptibility. *Geophys. J. Int.* **133**, 201–206 (1998).

61. Howard, D. L. et al. The XFM beamline at the Australian Synchrotron. *J. Synchrotron Radiat.* **27**, 1447–1458 (2020).

62. Sandeep Kumar, T. K. et al. Investigation of magnetite oxidation kinetics at the particle scale. *Metall. Mater. Trans. B* **50**, 150–161 (2018).

63. De Faria, D., Venâncio Silva, S. & De Oliveira, M. Raman microspectroscopy of some iron oxides and oxyhydroxides. *J. Raman Spectrosc.* **28**, 873–878 (1997).

64. Fauria, K. E. & Manga, M. Pyroclast cooling and saturation in water. *J. Volcanol. Geotherm. Res.* **362**, 17–31 (2018).

65. Dellino, P. et al. The analysis of the influence of pumice shape on its terminal velocity. *Geophys. Res. Lett.* **32**, L21306 (2005).

66. Reynolds, M. & Best, J. *The Tuluman Volcano, St. Andrew Strait, Admiralty Islands*. (Bureau of Mineral Resources, Geology and Geophysics, 1957).

67. Melson, W. G., Jarosewich, E. & Lundquist, C. A. Volcanic eruption at Metis Shoal, Tonga, 1967-1968: description and petrology. *Smithsonian Contributions to the Earth Sciences* (1970).

68. Hammer, J. E., Cashman, K. V., Hoblitt, R. & Newman, S. Degassing and microlite crystallization during pre-climactic events of the 1991 eruption of Mt. Pinatubo, Philippines. *Bull. Volcanol.* **60**, 355–380 (1999).

69. Shea, T. Bubble nucleation in magmas: A dominantly heterogeneous process? *J. Volcanol. Geothermal Res.* **343**, 155–170 (2017).

70. Matsumoto, K. & Geshi, N. Shallow crystallization of eruptive magma inferred from volcanic ash microtextures: a case study of the 2018 eruption of Shinmoedake volcano, Japan. *Bull. Volcanol.* **83**, 1–14 (2021).

71. Dürig, T. et al. Deep-sea eruptions boosted by induced fuel–coolant explosions. *Nat. Geosci.* **13**, 498–503 (2020).

72. Iezzi, G. et al. Deep sea explosive eruptions may be not so different from subaerial eruptions. *Sci. Rep.* **10**, 1–11 (2020).

73. Dürig, T. et al. Deep-sea fragmentation style of Havre revealed by dendrogrammatic analyses of particle morphometry. *Bull. Volcanol.* **82**, https://doi.org/10.1007/s00445-020-01408-1 (2020).

74. Cahalan, R. & Dufek, J. Explosive submarine eruptions: the role of condensable gas jets in underwater eruptions. *J. Geophys. Res.: Solid Earth* **126**, e2020JB020969 (2021).

75. Howard, D. L. et al. The XFM beamline at the Australian Synchrotron. *J. Synchrotron Radiat.* **27**, 1447–1458 (2020).

76. Ryan, C. G. et al. The maia detector and event mode. *Synchrotron Radiat. News* **31**, 21–27 (2018).

77. Ryan, C. G. & Jamieson, D. N. Dynamic analysis: on-line quantitative PIXE microanalysis and its use in overlap-resolved elemental mapping. *Nucl. Instrum. Methods Phys. Res. B.* **77**, 203–214 (1993).

78. Schindelin, J. et al. Fiji: an open-source platform for biological-image analysis. *Nat. Methods* **9**, 676–682 (2012).

79. Knafelc, J. et al. The effect of oxidation on the mineralogy and magnetic properties of olivine. *Am. Min.* **104**, 694–702 (2019).

80. Kraft, S., Stümpel, J., Becker, P. & Kuetgens, U. High resolution x-ray absorption spectroscopy with absolute energy calibration for the determination of absorption edge energies. *Rev. Sci. Instrum.* **67**, 681–687 (1996).

Acknowledgements

Author contributions

J.K., S.B., M.J., and D.G. interpreted the data and wrote the initial manuscript. J.K., S.B., M.J., and G.M. and D.H. designed and undertook the XFM and Fe-XANES experiments at the Australian Synchrotron. M.J. analysed the XFM data. M.J. and A.B. analysed the XANES data. J.K. designed and undertook the atmospheric oven heating experiments. H.C. conducted the EPMA analysis. E.F. conducted magnetic analysis. All authors contributed to refining the manuscript.

Competing interests

The authors declare no competing interests.

Additional information